

# Chemical environments of 6.7 GHz methanol maser sources

Sonu Tabitha Paulson,<sup>1\*</sup> Jagadheep D. Pandian<sup>1†</sup>

<sup>1</sup>*Department of Earth and Space Sciences, Indian Institute of Space Science & Technology, Thiruvananthapuram 695547, Kerala, India*

Accepted 2021 November 2. Received 2021 October 29; in original form 2021 March 19

## ABSTRACT

6.7 GHz methanol masers are the brightest of class II methanol masers that are regarded as excellent signposts in the formation of young massive stars. We present here a molecular line study of 68 6.7 GHz methanol maser hosts chosen from the MMB catalogue, that have MALT90 data available. We performed (1) pixel-by-pixel study of 9 methanol maser sources that have high signal-to-noise ratio and (2) statistical study taking into account the entire 68 sources. We estimated the molecular column densities and abundances of  $\text{N}_2\text{H}^+(1-0)$ ,  $\text{HCO}^+(1-0)$ ,  $\text{HCN}(1-0)$  and  $\text{HNC}(1-0)$  lines. The derived abundances are found to be in congruence with the typical values found towards high mass star forming regions. We derived the column density and abundance ratios between these molecular species as an attempt to unveil the evolutionary stage of methanol maser sources. We found the column density and abundance ratio of HCN to HNC to increase and that of  $\text{N}_2\text{H}^+$  to  $\text{HCO}^+$  to decline with source evolution, as suggested by the chemical models. The  $\text{HCN}/\text{HNC}$ ,  $\text{N}_2\text{H}^+/\text{HCO}^+$ ,  $\text{HNC}/\text{HCO}^+$  and  $\text{N}_2\text{H}^+/\text{HNC}$  ratios of the methanol maser sources are consistent with them being at a later evolutionary state than quiescent phase and possibly protostellar phase, but at an earlier stage than H II regions and PDRs.

**Key words:** masers – Stars – stars: formation

## 1 INTRODUCTION

High mass stars play a cardinal role in the evolution of galaxies by enriching the interstellar medium through stellar winds and supernovae. Understanding the formation of such stars in the Universe is therefore crucial for constraining the models of galaxy formation and evolution. In spite of this, high mass star formation still remains an elusive phenomenon and requires detailed exploration. We can attribute this to rapid formation which takes place while they are deeply embedded in dense clumps. This in itself introduces challenges in understanding their early formation phases, in addition to rarity and large distance scales.

One of the methods to probe the early evolutionary phases of high mass star formation is to make use of interstellar masers, among which class II methanol masers (the 6.7 GHz line being the brightest) are seen almost exclusively towards massive star forming regions (e.g., Menten et al. 1992; Xu et al. 2008; Breen et al. 2013, and references therein). There is strong evidence that 6.7 GHz methanol masers trace a very early stage of massive star formation (e.g., Minier et al. 2001; Ellingsen 2006; Pandian et al. 2010; Billington et al. 2019, and references therein). Since the chemical composition in star forming environments is highly sensitive to the physical conditions (Gerner et al. 2014), it is of interest to examine whether the chemical properties of the methanol maser hosts are in accordance with them tracing an early phase of massive star formation. Although there have been many studies that focus on the chemistry of high mass star forming regions (e.g. Sanhueza et al. 2012; Hoq et al. 2013; Miettinen

2014; Zhang et al. 2016), chemical processes surrounding 6.7 GHz methanol maser hosts are not much discussed yet. For example, Saral et al. (2018) investigated the physical and chemical properties of 30 high mass star forming clumps, the chemistry of which was traced using four molecular species:  $\text{N}_2\text{H}^+$ ,  $\text{HCO}^+$ , HCN and HNC. This was used to classify the clumps into protostellar candidates, young stellar objects (YSOs), and massive star forming regions (MSF), the latter containing H II regions, radio bright sources and methanol masers.

The MALT90 survey (Jackson et al. 2013) carried out a comprehensive study of molecular emission towards 3246 high-mass clumps detected in the ATLASGAL survey. It was found that ratios of integrated line intensities of several molecules such as  $\text{HCO}^+/\text{HNC}$  and  $\text{HCN}/\text{HNC}$  showed systematic variation with the evolutionary stage of the source (Rathborne et al. 2016). A similar study targeting a much wider range of molecules towards  $\sim 600$  high mass clumps, was performed by Urquhart et al. (2019). They also discovered that several line ratios were probes of the evolutionary state of the source. However, a direct comparison to chemical models is not possible since the studies of both Rathborne et al. (2016) and Urquhart et al. (2019) focused on integrated line intensities rather than column densities. Since the column density shows additional dependence on the excitation temperature and the optical depth, one needs to carry out radiative transfer modelling of the molecular spectra in order to compare the results with chemical models. Since all the studies focused on the evolutionary state in the context of massive star formation, there is a lack of proper knowledge on the chemistry of methanol maser sources alone.

In Paulson & Pandian (2020) (hereafter Paper I), we analysed the evolutionary stage of 320 sources associated with 6.7 GHz methanol

\* E-mail: sonutabitha.15@res.iist.ac.in

† E-mail: jagadheep@iist.ac.in

masers using spectral energy distributions of dust continuum maps. We concluded that while a majority of our sources are more evolved as compared to infrared dark clouds, they are still in an early evolutionary stage, with the mass to luminosity ratio being consistent with the sources being in accretion phase. In this paper, we use the MALT90 data to conduct molecular studies of 68 6.7 GHz methanol maser sources and investigate whether the evolutionary phase of methanol maser hosts inferred from chemical signatures aligns with results in Paper I.

The structure of the paper is as follows. In Section 2, we discuss the source selection and data analysis. The results of our study are presented in Section 3. A detailed discussion of the results in the context of the evolutionary phase of 6.7 GHz methanol maser hosts is presented in Section 4, and we summarize our results in Section 5.

## 2 SOURCE SELECTION AND DATA ANALYSIS

### 2.1 MALT90 Data

The source sample of the present paper was chosen among the sources studied in Paper I, that have MALT90 data available. The MALT90 survey aims at characterizing the physical and chemical properties of massive star formation in our Galaxy. The survey is targeted towards 2014 compact sources detected in the ATLASGAL survey (Schuller et al. 2009) covering Galactic longitude ranges  $300^\circ < l < 357^\circ$  and  $3^\circ < b < 20^\circ$ , with the Mopra Spectrometer (MOPS)<sup>1</sup> arrayed on the Mopra 22 m telescope. The survey obtained  $3' \times 3'$  maps around each source covering a total of 3264 high-mass clumps. MALT90 has mapped 16 molecular lines simultaneously at frequencies near 90 GHz with a velocity resolution of  $0.11 \text{ km s}^{-1}$ . The 16 spectral lines and their rest frequencies are shown in Table 1 (Jackson et al. 2013). The beam size of Mopra is  $38''$  at 86 GHz, with a main beam efficiency of 0.49 (Ladd et al. 2005). Among the 320 sources listed in Paper I, 138 of them were found to be included in the MALT90 survey. We have further narrowed down our study to sources that have strong detections ( $S/N \geq 3$  in the moment zero map) in  $\text{HCO}^+(1-0)$ ,  $\text{HCN}(1-0)$ ,  $\text{HNC}(1-0)$  and  $\text{N}_2\text{H}^+(1-0)$ . These molecular transitions are considered the brightest of the transitions covered by the MALT90 survey and have shown to be good tracers of density. In order to verify the association of the methanol masers with the MALT90 clump, we have compared the peak velocity of maser emission with that of molecular emission from the clump. We find that the velocity offsets are less than  $10 \text{ km s}^{-1}$ , with the mean offset being  $3 \text{ km s}^{-1}$ , which is similar to that observed in earlier studies (e.g. Billington et al. 2019). We investigated the spatial matching of methanol maser sites and MALT90 clumps by analysing the differences in their positions, obtained from their catalogues. If the angular offset was found to be less than half of the MALT90 beam size, the maser is considered to be physically associated with the clump. If more than one clump is found to be matched with a particular maser, we chose the clump having the least angular offset as the physically associated one. The angular offsets between maser sites and clumps for the 68 MM sources were typically less than 6 arcseconds. This suggests that all the methanol masers in this study are indeed physically associated with the MALT90 clumps.

The molecular line modelling was performed in CASSIS (Caux

et al. 2011), under the assumption of local thermodynamic equilibrium (LTE). CASSIS gives the best fit estimates for molecular column density, excitation temperature, line width and LSR velocity based on the initial parameters provided for the same. The values of initial parameters are obtained by fitting the spectra using the CLASS program of the GILDAS<sup>2</sup> software package. Prior to the fitting, the spectrum of each pixel in the data cube is extracted and data were converted from antenna temperatures to main beam temperatures by dividing it by main beam efficiency ( $\eta = 0.49$ ). For the molecules that exhibit hyperfine components ( $\text{HCN}$  and  $\text{N}_2\text{H}^+$ ), fitting is performed using method HFS (hyperfine-structure fit). For the molecules that do not have hyperfine satellites ( $\text{HCO}^+$  and  $\text{HNC}$ ), method GAUSS<sup>3</sup> (Gaussian fit) is employed. The fit performed using method HFS gives the optical depth in addition to the LSR velocity and FWHM of the spectral line, while the method GAUSS gives an estimate of only the latter two parameters. We estimate the excitation temperature of the line using the antenna equation

$$T_{mb} = f[J(T_{ex}) - J(T_{bg})](1 - e^{-\tau_\nu}) \quad (1)$$

where  $T_{mb}$  is the main beam temperature,  $f$  is the filling factor,  $\tau_\nu$  is the optical depth of the line,  $T_{bg}$  is the background temperature, and  $J(T)$  is defined by

$$J(T) = \frac{h\nu}{k} \frac{1}{e^{h\nu/kT} - 1} \quad (2)$$

For lines whose optical depth is known through fitting of hyperfine structure, equation (1) can be used to determine the excitation temperature. The excitation temperature can also be determined for lines that are known to be very optically thick by assuming  $\tau$  to be infinity in equation (1). For the molecules that do not possess hyperfine transitions, we followed the method described in Sanhueza et al. (2012) to estimate the optical depths. The process essentially involves computing the ratio of peak main beam temperatures of an optically thick and optically thin line and then equating it with the ratio of their optical depths. Once we obtain the optical depths, we estimate their excitation temperatures using equation (1).

In order to study the chemical evolution within the maser host, we performed a pixel-by-pixel SED fitting of molecular data cubes. For this purpose, we chose sources where at least 30 pixels in the moment zero map of MALT90, have  $S/N$  ratio  $\geq 5$ . This results in a sample of 9 sources that are used for what we refer to as the ‘‘pixel-by-pixel analysis’’. We also aim to study properties of methanol maser hosts from a chemical perspective compared to sources belonging to different evolutionary stages. Since this cannot be accomplished with just 9 sources, we expanded our source sample to the ones where the brightest pixel in the moment zero map has  $S/N > 3$ . It is to be noted that the peak signal to noise ratio of individual spectra are much higher since the moment zero map is obtained from the total intensity of the full spectrum of the spectrometer sub-band, with most spectral channels being devoid of any signal. We call this as the statistical analysis of maser sources. 59 sources, apart from the 9 sources listed above, were chosen for the latter approach. In total, our sample constitutes of 68 6.7 GHz methanol maser sources (hereafter MM sources), where we carry out a pixel-by-pixel analysis (approach I) for 9 sources and a statistical analysis (approach II) for the entire source sample. A comparison of the distances and methanol maser luminosities of our sample with that of the 320 sources in Paper I as well as the 972 sources in the entire MMB

<sup>1</sup> The University of New South Wales Digital Filter Bank used for the observations with the Mopra Telescope was provided with support from the Australian Research Council.

<sup>2</sup> <http://www.iram.fr/IRAMFR/GILDAS>

<sup>3</sup> A detailed description of method HFS and method GAUSS can be found here, <http://www.iram.fr/IRAMFR/GILDAS/doc/html/classhtml/class.html>

**Table 1.** Spectral lines in MALT90 survey

Transition	Frequency (MHz)	Tracer
HCO <sup>+</sup> (1–0)	89188.526	Density; Kinematics
H <sup>13</sup> CO <sup>+</sup> (1–0)	86754.330	Optical depth, Column density, $V_{LSR}$
N <sub>2</sub> H <sup>+</sup> (1–0)	93173.772	Density, chemically robust
HCN (1–0)	88631.847	Density
HNC(1–0)	90663.572	Density; Cold chemistry
<sup>13</sup> CS (2–1)	92494.303	Optical depth, Column density, $V_{LSR}$
CH <sub>3</sub> CN 5(0)–4(0)	91987.086	Hot core
HC <sub>3</sub> N (10–9)	90978.989	Hot core
<sup>13</sup> C <sup>3</sup> 4S (2–1)	90926.036	Optical depth, Column density, $V_{LSR}$
HC <sup>13</sup> CCN (10–9)	90593.059	Hot core
HNCO 4(1,3)–3(1,2)	88239.027	Hot core
HNCO 4(0,4)–3(0,3)	87925.238	Hot core
C <sub>2</sub> H (1–0) 3/2–1/2	87316.925	Photodissociation region
HN <sup>13</sup> C (1–0)	87090.859	Optical depth, Column density, $V_{LSR}$
SiO (1–0)	86847.010	Shock/outflow

MMB names	ATLASGAL names	MMB names	ATLASGAL names
G006.189-0.358	AGAL006.188-00.357	G338.497+0.207	AGAL338.497+00.207
G010.724-0.334	AGAL010.724-00.332	G338.566+0.110	AGAL338.567+00.109
G010.958+0.022	AGAL010.957+00.022	G338.850+0.409	AGAL338.851+00.409
G011.034+0.062	AGAL011.034+00.061	G339.282+0.136	AGAL339.283+00.134
G012.625-0.017	AGAL012.623-00.017	G339.476+0.185	AGAL339.476+00.184
G012.889+0.489	AGAL012.888+00.489	G339.582-0.127	AGAL339.584-00.127
G013.179+0.061	AGAL013.178+00.059	G339.622-0.121	AGAL339.623-00.122
G014.631-0.577	AGAL014.632-00.577	G340.249-0.046	AGAL340.249-00.046
G305.799-0.245	AGAL305.799-00.244	G340.785-0.096	AGAL340.784-00.097
G309.384-0.135	AGAL309.384-00.134	G341.218-0.212	AGAL341.217-00.212
G311.947+0.142	AGAL311.947+00.142	G341.276+0.062	AGAL341.274+00.061
G324.923-0.568	AGAL324.923-00.569	G346.480+0.221	AGAL346.481+00.221
G326.608+0.799	AGAL326.607+00.799	G346.481+0.132	AGAL346.481+00.131
G326.859-0.677	AGAL326.859-00.677	G347.628+0.149	AGAL347.627+00.149
G329.469+0.503	AGAL329.469+00.502	G348.884+0.096	AGAL348.886+00.097
G330.283+0.493	AGAL330.284+00.492	G349.092+0.105	AGAL349.091+00.106
G331.134+0.156	AGAL331.134+00.156	G350.015+0.433	AGAL350.016+00.432
G331.342-0.346	AGAL331.342-00.347	G350.520-0.350	AGAL350.521-00.349
G331.442-0.187	AGAL331.442-00.187	G350.686-0.491	AGAL350.687-00.491
G331.710+0.603	AGAL331.709+00.602	G351.688+0.171	AGAL351.689+00.172
G332.295-0.094	AGAL332.296-00.094	G352.604-0.225	AGAL352.604-00.226
G332.364+0.607	AGAL332.364+00.604	G352.855-0.201	AGAL352.856-00.202
G332.560-0.148	AGAL332.559-00.147	G354.615+0.472	AGAL354.616+00.472
G332.942-0.686	AGAL332.942-00.686	G354.724+0.300	AGAL354.724+00.301
G333.163-0.101	AGAL333.161-00.099	G355.538-0.105	AGAL355.538-00.104
G333.387+0.032	AGAL333.386+00.032	G013.657-0.599 <sup>a</sup>	AGAL013.658-00.599
G336.809+0.119	AGAL336.808+00.119	G318.948-0.196 <sup>b</sup>	AGAL318.948-00.197
G336.957-0.225	AGAL336.958-00.224	G326.474+0.703 <sup>c</sup>	AGAL326.474+00.702
G336.958-0.977	AGAL336.958-00.977	G327.393+0.199 <sup>d</sup>	AGAL327.393+00.199
G337.097-0.929	AGAL337.098-00.929	G330.876-0.384 <sup>e</sup>	AGAL330.876-00.384
G337.201+0.114	AGAL337.201+00.114	G333.314+0.105 <sup>f</sup>	AGAL333.314+00.106
G337.258-0.101	AGAL337.258-00.101	G335.586-0.289 <sup>g</sup>	AGAL335.586-00.291
G337.300-0.874	AGAL337.301-00.874	G338.281+0.541 <sup>h</sup>	AGAL338.281+00.542
G337.632-0.079	AGAL337.632-00.079	G353.463+0.563 <sup>i</sup>	AGAL353.464+00.562

**Table 2.** The MMB and ATLASGAL names of the 68 sources studied in this paper. The nine sources considered for pixel-by-pixel study are indicated by alphabets *a* to *i*. These nine sources are referred to as G13, G318, G326, G327, G330, G333, G335, G338 and G353 respectively

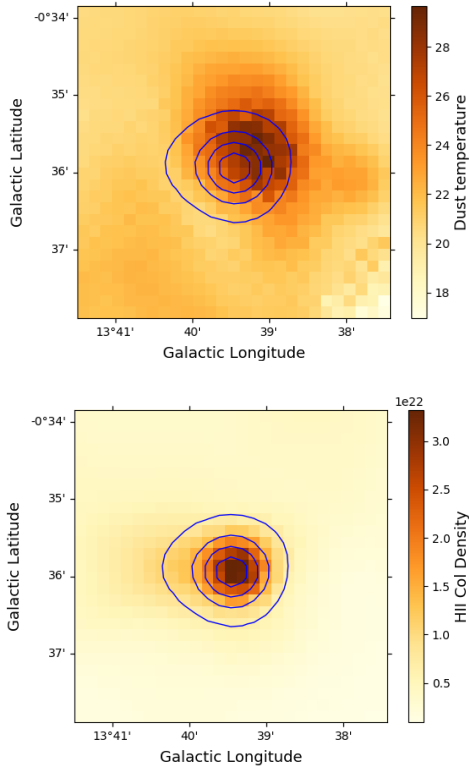


**Figure 1.** An example of temperature (top) and  $\text{H}_2$  column density (bottom) maps obtained by pixel-by-pixel fitting of dust continuum data for the source G13. The SPIRE 250  $\mu\text{m}$  emission is overlaid as contours.

catalogue shows our sample to be representative of the methanol maser population in the Galaxy with no systematic biases being introduced by our sample selection procedure (see Appendix B). The MMB names and ATLASGAL names of the entire sample of sources are listed in Table 2. Among the 68 maser sources, we have 51  $\text{N}_2\text{H}^+$  detections, 59  $\text{HCO}^+$ , 57  $\text{HNC}$  and 52  $\text{HCN}$  detections.

## 2.2 Dust continuum data

The molecular abundance is calculated by dividing the molecular column density by the  $\text{H}_2$  column density. The  $\text{H}_2$  column density is determined using the spectral energy distribution of the dust continuum emission. We made use of the 70, 160  $\mu\text{m}$  (PACS) as well as 250, 350 and 500  $\mu\text{m}$  (SPIRE) data, observed as a part of the Herschel infrared Galactic plane survey (Hi-GAL, [Molinari et al. \(2010\)](#)). The 870  $\mu\text{m}$  data is obtained from the ATLASGAL survey ([Schuller et al. 2009](#)). The maps at different wave bands have different data units, resolution and plate scales. Moreover, in order to calculate the molecular abundances, it is important to ensure that the  $\text{H}_2$  column densities are determined at the same world coordinates as that of the MALT90 data. We hence processed the data using the Herschel Interactive Processing Environment (HIPE)<sup>4</sup> using the following steps: Firstly, the surface brightness unit of all the images were converted to  $\text{Jy pixel}^{-1}$  using the task ‘Convert Image Unit’. The data were then projected onto a common grid, with the pixel size and resolution of the MALT90 data cube. This made sure that

<sup>4</sup> <http://herschel.esac.esa.int/hipe/>

each coordinate of the dust continuum map corresponds to the same location in the MALT90 data cube. The plug-in ‘Photometric Convolution’ is used for this purpose. A constant background, estimated from the mean continuum in a region devoid of source emission, was then subtracted from the data. The pixels were then fit using the standard grey body model. We derive the hydrogen column density ( $N(\text{H}_2)$ ) using the equations discussed in Paper I. The maps obtained for source G13 is shown in Fig. 1 as an example.

For the pixel-by-pixel analysis, we modelled the spectra corresponding to each pixel of the MALT90 data cube and then compared with the dust temperatures and  $\text{H}_2$  column densities of same pixels obtained by pixel-by-pixel SED fitting of dust continuum maps. For the statistical study, we modelled the brightest pixel in the molecular data cube (brightest in the moment zero map) and compared with the  $\text{H}_2$  column density corresponding to that pixel. The dust temperatures for the latter are taken from Paper I.

## 3 RESULTS

We present the results obtained from pixel-by-pixel study as well as the statistical study of the sources. We mainly focus on the column densities and abundances of molecules obtained after line modelling. We also briefly account for the integrated line intensities of the molecular emissions. The uncertainties in the column densities and abundances obtained are typically less than 20 percent.

### 3.1 Dust temperatures and $\text{H}_2$ column densities

The dust temperatures obtained after pixel-by-pixel SED fitting ranges from 13 K to 49 K with a mean value 24 K. The  $\text{H}_2$  column densities derived for each pixel lie in the range,  $(0.16 - 10.4) \times 10^{22} \text{ cm}^{-2}$  with an average value of  $2.68 \times 10^{22} \text{ cm}^{-2}$ . For the statistical analysis, the dust temperature (taken from Paper I) ranges between 13 K and 36 K with a mean value of 23 K and the  $\text{H}_2$  column densities lie in the range  $(0.25 - 6.98) \times 10^{22} \text{ cm}^{-2}$  with an average value of  $1.86 \times 10^{22} \text{ cm}^{-2}$ . These values are comparable to what are typically seen in massive star forming regions. For example, the dust temperature and  $\text{H}_2$  column density values derived by [Hoq et al. \(2013\)](#) for 332 high mass clumps are 6.7–41.5 K (22 K on average) and  $(0.2 - 93.99) \times 10^{22} \text{ cm}^{-2}$  ( $4.89 \times 10^{22} \text{ cm}^{-2}$  on average) respectively. The dust temperature values are also consistent with what have been reported by [Guzman et al. \(2015\)](#) for MALT90 clumps (See Appendix C).

### 3.2 Optical depths and excitation temperatures

The fits to the hyperfine structure of  $\text{HCN}$  (1–0) show the line to be optically thick with typical values of  $\tau$  being greater than 5. In contrast,  $\text{N}_2\text{H}^+$  (1–0) was found to be typically optically thin, with the optical depth ranging from 0.1 to 1.2 and a mean value of 0.3. We derived the optical depths for  $\text{HCO}^+$  and  $\text{HNC}$  lines using the optically thin  $\text{N}_2\text{H}^+$  line, as their optically thin isotopologues ( $\text{H}^{13}\text{CO}^+$  and  $\text{HN}^{13}\text{C}$ ) were undetected in our sources and found both lines to be optically thick. The excitation temperatures calculated for  $\text{HCN}$ , ranges from 4 to 10 K. We employed the same excitation temperatures for modelling  $\text{HNC}$  as well, as the  $\text{HCN}$  and  $\text{HNC}$  molecules show a tight correlation in their integrated intensity. The two molecules are also observed to have formed via similar chemical channels. The excitation temperatures of  $\text{HCO}^+$  and  $\text{N}_2\text{H}^+$  range from 6–12 K and 17–30 K respectively.

**Table 3.** Column densities and abundances.

Quantity	Min	Max	Mean	Std.	Median
$N_I(\text{HCN})$	7.56(12)	9.77(13)	3.39(13)	1.97(13)	2.98(13)
$X_I(\text{HCN})$	1.51(-10)	1.32(-8)	1.74(-9)	1.81(-9)	1.29(-9)
$N_{II}(\text{HCN})$	1.20(13)	1.06(14)	3.21(13)	2.11(13)	2.66(13)
$X_{II}(\text{HCN})$	1.68(-10)	1.06(-8)	2.27(-9)	2.05(-9)	1.56(-9)
$N_I(\text{HNC})$	1.59(12)	1.57(14)	2.14(13)	1.95(13)	1.45(13)
$X_I(\text{HNC})$	4.49(-11)	2.45(-8)	1.47(-9)	1.70(-9)	1.14(-9)
$N_{II}(\text{HNC})$	5.25(12)	8.89(13)	2.12(13)	5.76(12)	1.83(13)
$X_{II}(\text{HNC})$	2.24(-10)	4.64(-9)	1.28(-9)	8.27(-10)	9.47(-10)
$N_I(\text{HCO}^+)$	2.72(12)	9.69(13)	1.83(13)	1.81(13)	1.20(13)
$X_I(\text{HCO}^+)$	1.76(-10)	1.53(-8)	1.37(-9)	1.81(13)	1.06(-9)
$N_{II}(\text{HCO}^+)$	4.36(12)	4.82(13)	1.80(13)	1.16(13)	1.42(13)
$X_{II}(\text{HCO}^+)$	1.35(-10)	4.79(-9)	1.26(-9)	1.00(-9)	9.61(-10)
$N_I(\text{N}_2\text{H}^+)$	5.29(12)	9.25(13)	2.97(13)	1.72(13)	2.50(13)
$X_I(\text{N}_2\text{H}^+)$	1.33(-10)	7.84(-9)	1.85(-9)	1.41(-9)	1.42(-9)
$N_{II}(\text{N}_2\text{H}^+)$	2.31(11)	6.84(13)	2.97(13)	1.51(13)	2.48(13)
$X_{II}(\text{N}_2\text{H}^+)$	1.58(-11)	4.09(-9)	1.81(-9)	1.01(-9)	1.53(-9)

a(b) indicates  $\times 10^b$ . N and X represents column density and abundance respectively. Subscripts I and II indicates pixel-by-pixel study and statistical study.

**Table 4.** Spearman correlation coefficients.

Molecules	Pix-by-pix	Stat
HCN	-0.62	-0.64
HNC	-0.53	-0.54
HCO <sup>+</sup>	-0.61	-0.62
N <sub>2</sub> H <sup>+</sup>	-0.61	-0.55

Correlation coefficients between different molecular species and H<sub>2</sub> column densities for pixel-by-pixel study and statistical study.

### 3.3 Anomalies in the HCN spectra

Most of the HCN spectra modelled in this work exhibit anomalous and asymmetric line profiles. The complex line profiles are mostly due to hyperfine anomalies observed in the  $J = 1 - 0$  line, and also in part due to complex motions within the source. Anomalies in the hyperfine structure of HCN have been observed by several authors to date (Guilloteau & Baudry 1981; Loughnane et al. 2012; Mullins et al. 2016). The  $J = 1 - 0$  transition of HCN has three hyperfine lines ( $F = 1 - 0, 1 - 1$  and  $2 - 1$ ). Under LTE conditions, the ratios of the relative intensities of the two nearby hyperfine lines of HCN(1-0), are in the form 1:5:3. If the spectrum is anomalous, we observe a boosted  $F = 0 - 1$  hyperfine line. This line can also be broader than the rest of the hyperfine components. Fig. 2 shows an example of an anomalous HCN spectrum taken from our sample. While the anomalous spectra could in principle be modelled using non-LTE radiative transfer codes such as MOLFIT (Möller et al. 2017), such an analysis is beyond the scope of our present work. We have modelled the HCN spectra by fitting the  $F = 1 - 1$  and  $2 - 1$  components under assumption of LTE. The poor fit to the  $F = 0 - 1$  hyperfine line is likely to lead to systematic uncertainties in the derived column densities. In order to account for this, we calculated the ratios of area under the hyperfine satellites of the spectrum and the fit. In almost all the cases, the area under the CASSIS fit is  $\sim 20\%$  less than area under the actual spectrum. Hence, we infer that the column densities obtained for HCN are underestimated by 20%.

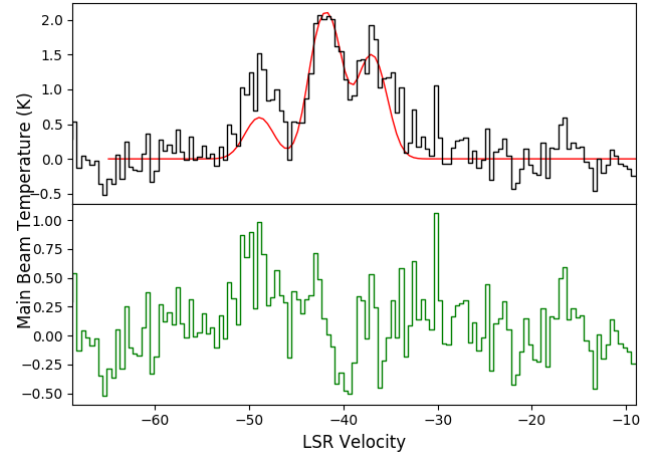


**Figure 2.** An anomalous HCN line profile. The fit obtained (assuming LTE) is shown in red. The fit residual is marked in green.

### 3.4 Molecular column densities and abundances

Table 3 shows the minimum, maximum, mean and median values of molecular column densities and abundances for both the pixel-by-pixel and statistical methods (indicated by I and II respectively). We can see that the column densities and abundances obtained from two methods are very similar to each other. Miettinen (2014) reports a similar range for HCN, HNC, HCO<sup>+</sup> and N<sub>2</sub>H<sup>+</sup> column densities and abundances for their sample of 35 massive clumps, though their mean HCN and N<sub>2</sub>H<sup>+</sup> column density is an order of magnitude higher than our values. While the N<sub>2</sub>H<sup>+</sup> column densities and abundances for all the 51 sources fall in a range similar to that reported by Hoq et al. (2013) and Saral et al. (2018), the HCO<sup>+</sup> column densities show some deviations. The HCO<sup>+</sup> column densities derived by Hoq et al. (2013) for their sample of 333 massive clumps,  $(0.4 - 35.8) \times 10^{14} \text{ cm}^{-2}$  ( $3.57 \times 10^{14} \text{ cm}^{-2}$  on average), are an order of magnitude higher than those derived for our sources. On the other hand, the median value of HCO<sup>+</sup> abundance of our sample ( $1.09 \times 10^{-9}$ ) is found to be higher than that observed by Zhang et al. (2016) for their sources categorised as H II regions/PDRs ( $3 \times 10^{-10}$ ). The mean HCO<sup>+</sup> column density

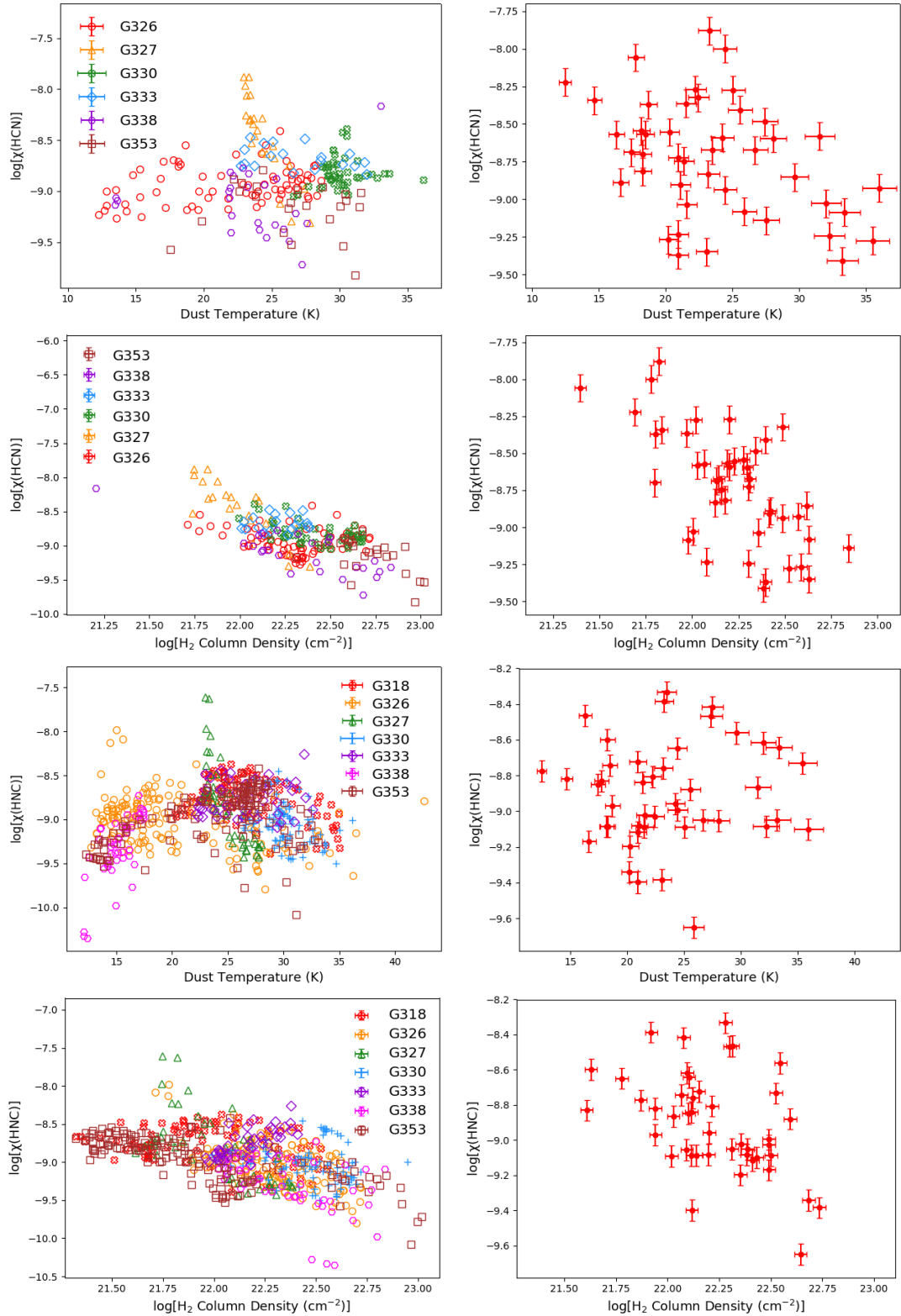


**Figure 3.** Variation of HCN abundance ( $X(\text{HCN})$ ) with respect to dust temperature and  $\text{H}_2$  column density. The first and third panel show the plots for pixel-by-pixel study whereas the second and fourth panel depict the results for statistical study. For the pixel-by-pixel case, only a characteristic error bar is shown in its top corner for the sake of clarity.

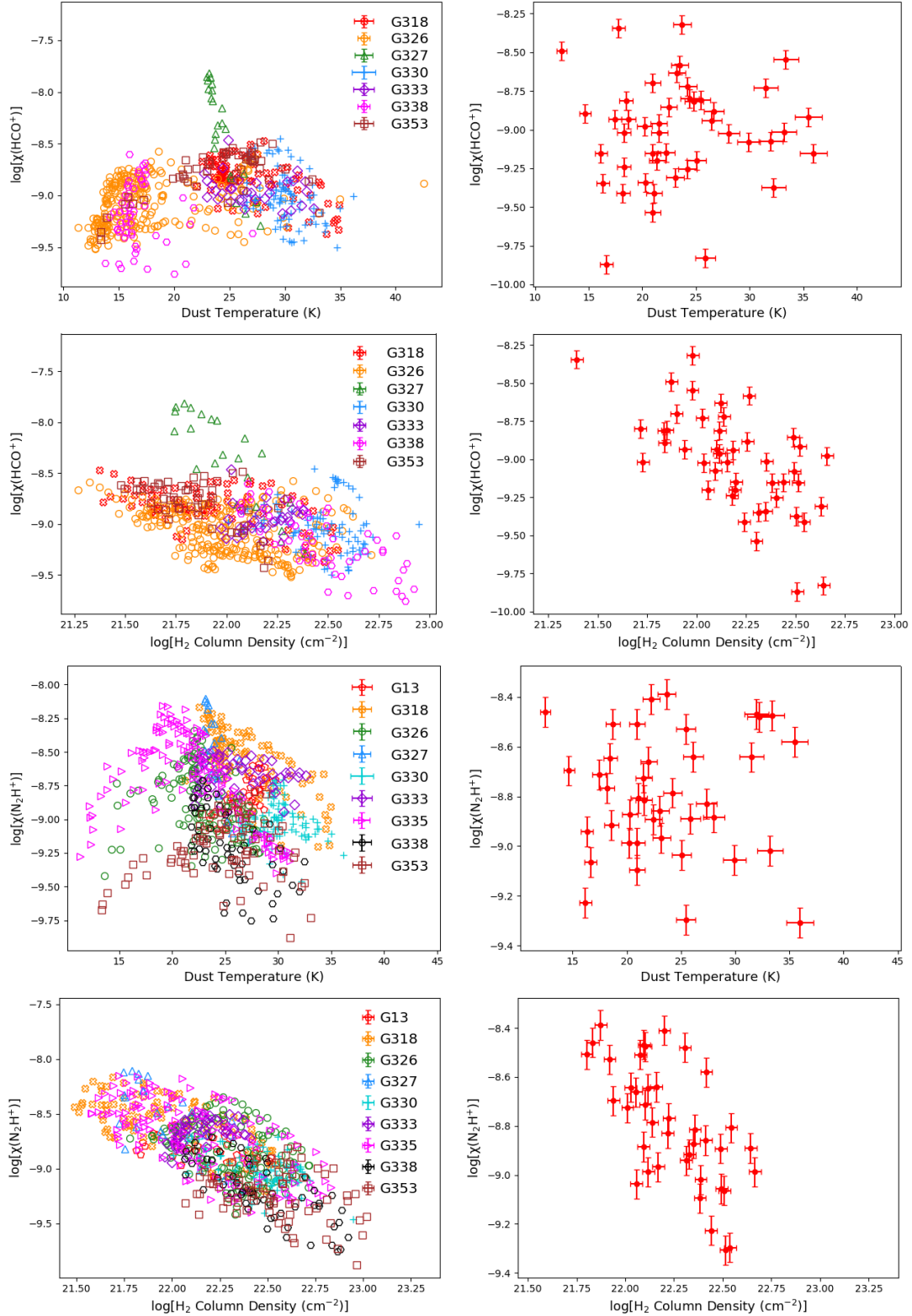


**Figure 4.** Variation of HNC abundance ( $X(\text{HNC})$ ) with respect to dust temperature and  $\text{H}_2$  column density. The first and third panel show the plots for pixel-by-pixel study whereas the second and fourth panel depict the results for statistical study. For the pixel-by-pixel case, only a characteristic error bar is shown in its top-right corner for the sake of clarity.

value is also less than those derived by [Saral et al. \(2018\)](#) for their sample of YSOs and protostellar sources. This could be due to the differences in the methodology adopted for calculating the excitation temperature. [Zhang et al. \(2016\)](#) and [Hoq et al. \(2013\)](#) assume the excitation temperature to be equal to the dust temperature. [Saral et al. \(2018\)](#) on the other hand, derive excitation temperatures using the optical depth of  $\text{N}_2\text{H}^+$  and use the same for the optically thick lines:  $\text{HCO}^+$ ,  $\text{HCN}$  and  $\text{HNC}$ . In contrast, we find the excitation temperature of  $\text{HCO}^+$ ,  $\text{HCN}$  and  $\text{HNC}$  to be significantly lower compared to that of  $\text{N}_2\text{H}^+$ , and much less than the dust temperature.

Figures 3 and 4 show  $\text{HCN}$ ,  $\text{HNC}$ ,  $\text{HCO}^+$  and  $\text{N}_2\text{H}^+$  abundances plotted as a function of dust temperature and  $\text{H}_2$  column density. While there does not appear to be any trend of the molecular abundances with dust temperature, they appear to be negatively correlated with  $\text{H}_2$  column density. The correlation coefficients obtained from the Spearman correlation test performed on molecular abundances, and  $\text{H}_2$  column densities, are given in Table 4. We note that the trends shown by the abundances in the statistical study are also reflected in the pixel wise analysis. We also carried out Pearson correlation test on the sample of 68 MM sources for  $\text{HCN}$  and  $\text{HNC}$  abundances (with respect to  $\text{H}_2$  column density) and the coefficients obtained are -0.52 and -0.35 respectively. The Pearson correlation coefficient found between  $\text{HCN}$  abundance and  $\text{H}_2$  column density is very similar to that reported by [Miettinen \(2014\)](#), who found the correlation coefficient to be -0.55 for their sample. While [Hoq et al. \(2013\)](#) and [Miettinen \(2014\)](#) infer that  $\text{HCO}^+$  abundances tend to increase with evolution, we do not see any such trend in our data. It is to be noted that the inference of  $\text{HCO}^+$  abundance increasing with evolutionary stage was made by [Miettinen \(2014\)](#) assuming that the  $\text{H}_2$  column density increases with source evolution. This is, however, unlikely to be true since the observation of high  $\text{H}_2$  column density in single dish studies is more likely to be due to factors other than evolution, such as a larger physical source area being covered in a telescope beam for a more distant source. In contrast, the dust temperature is seen to be a much better probe of the evolutionary stage of the source, with temperatures seen in infrared dark clouds seen to be systematically lower than that in more evolved sources such as methanol masers and H II regions ([Giannetti et al. 2013](#)). The lack of any correlation between the dust temperature and  $\text{HCO}^+$  abundance thus casts doubt on the interpretation of [Miettinen \(2014\)](#) on the increase of  $\text{HCO}^+$  abundance with source evolution.

### 3.5 Integrated line intensities

Earlier studies (e.g., [Rathborne et al. 2016](#); [Urquhart et al. 2019](#)) have studied the chemistry in high-mass clumps using integrated line intensities and their ratios. The integrated line intensities divided by  $\text{H}_2$  column density have also been considered as a rough estimate of molecular abundance ([Urquhart et al. 2019](#)). However, this assumes that the physical conditions are similar for various transitions. In practice, different transitions have different excitation temperatures and optical depths, which result in a variation of the column density from a simple linear relation to the integrated intensity. To illustrate this, Fig. 5 shows the plot of integrated line intensity as a function of column density for  $\text{N}_2\text{H}^+$  and  $\text{HCO}^+$  molecules corresponding to MM sources in our study. The data points are colour-coded by the variation in optical depth. Fig. 5 shows that the sources exhibit a clear bifurcation between high and low optical depth values. The sources possessing lower  $\tau$  values tend to show a stronger linear correlation with scatter among these points arising from variations in the excitation temperature. On the other hand, sources with larger optical depth tend to show more dispersion. This implies that integrated

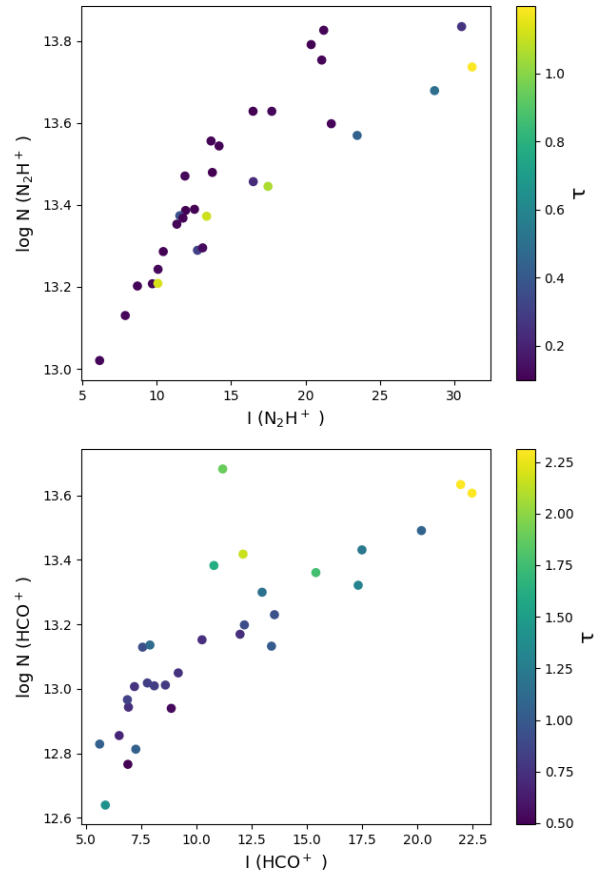


**Figure 5.** Column densities plotted against the integrated intensities of different molecules for MM sources. The colours indicate the variation in optical depth.

intensities are good proxies for column densities only for complex molecules with low optical depth, and studies that target optically thick molecules such as  $\text{HCN}$ ,  $\text{HNC}$  and  $\text{HCO}^+$  require radiative transfer modelling in order to obtain reliable column densities.

The  $\text{HCN}$  integrated intensities do not show any variation with the dust temperature. On the contrary, the integrated intensity of  $\text{HNC}$ , shows a weak positive correlation (Spearman correlation coefficient,  $r = 0.28$ ). This trend in  $\text{HNC}$  is in agreement with what is reported by [Zhang et al. \(2016\)](#) and [Urquhart et al. \(2019\)](#). The  $\text{HNC}$  line intensities divided by  $\text{H}_2$  column densities, on the other hand, show no discernible trend. The  $\text{HCO}^+$  line intensity displays a slight increasing trend with dust temperature ( $r = 0.32$ ), much in agreement with [Zhang et al. \(2016\)](#) and [Urquhart et al. \(2019\)](#). The integrated intensity of  $\text{HCO}^+$  divided by  $\text{H}_2$  column density show no obvious trends with dust temperature. This is contrary to what is inferred by [Urquhart et al. \(2019\)](#), where they detect a weak positive correlation with dust temperature. The integrated intensity of  $\text{N}_2\text{H}^+$  appears to be invariant with dust temperature. This result is in congruence with what is observed by [Urquhart et al. \(2019\)](#). [Zhang et al. \(2016\)](#) however, reports a slightly positive correlation. The ratio of integrated line intensity of  $\text{N}_2\text{H}^+$  to the  $\text{H}_2$  column density show no distinct trend with dust temperature, which is in good agreement with the results of [Urquhart et al. \(2019\)](#).



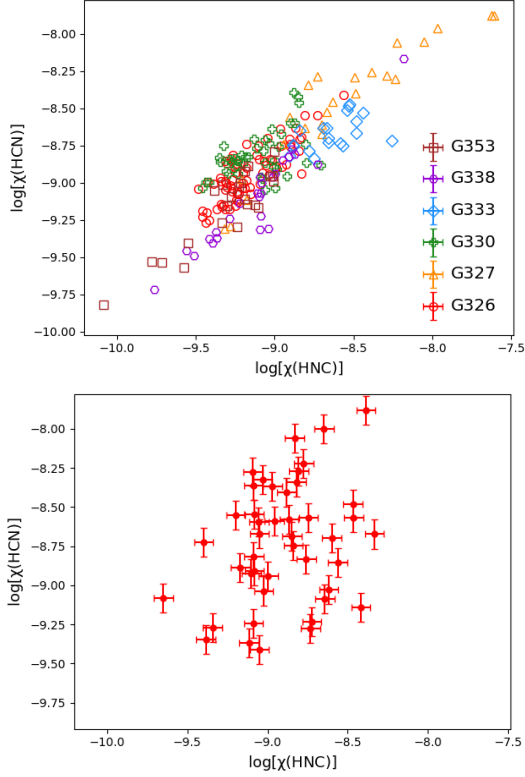


**Figure 6.**  $X(\text{HNC})$  Vs  $X(\text{HCN})$ . The top panel shows the plots for pixel-by-pixel study whereas the bottom panel depicts the results for statistical study. Pearson correlation coefficient for these two molecular species are 0.72 and 0.35, for pixel-by-pixel and statistical studies respectively.

## 4 DISCUSSION

In this section we discuss in detail the chemistry of different molecules based on the chemical models, followed by a brief discussion on the infall signatures observed in our sample. We also discuss the evolutionary status of methanol maser sources, gleaned from their molecular abundance and line integrated intensity ratios.

### 4.1 Comparison to chemical models

According to gas-phase chemical models, HCN and its metastable geometrical isomer HNC are primarily produced through the dissociative recombination reaction of  $\text{HCNH}^+$  as described in Appendix A1. Fig. 6 shows HCN abundance plotted as a function of HNC abundance. We can clearly see a strong positive correlation in the pixel-by-pixel case whereas there is more scatter in the statistical study. A Pearson correlation test carried out on the HNC and HCN abundances for the pixel-by-pixel analysis yields a correlation coefficient of 0.72 with 99.8% confidence level ( $p$ -value of 0.002)<sup>5</sup> For the statistical analysis, we obtained the Pearson correlation coefficient to be 0.35 ( $p$ -value of 0.0003). A similar positive correlation is observed by Miettinen (2014) (Pearson correlation coefficient being 0.45) for their statistical study of IRDCs. The abundance ratio between HCN and HNC is found to lie in the range 0.21 to 4.76 with

<sup>5</sup> Throughout the paper we have adopted a threshold of  $> 3\sigma$  confidence for claiming statistical significance, which corresponds to a  $p$ -value  $< 0.003$  for the null hypothesis of the two samples not being correlated.

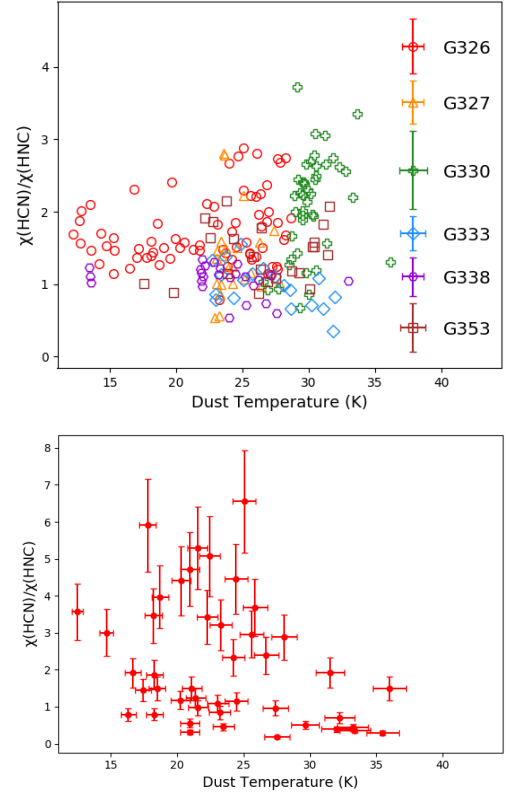


**Figure 7.**  $X(\text{HNC})/X(\text{HCN})$  vs dust temperature. The top panel (a) shows the plots for pixel-by-pixel study whereas the bottom panel (b) shows the results for statistical study.

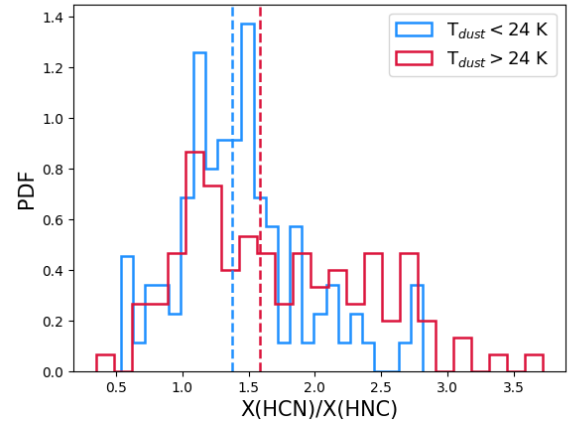


**Figure 8.** Probability density functions of HCN/HNC abundance ratios for  $T_{\text{dust}} > 24 \text{ K}$  and  $T_{\text{dust}} < 24 \text{ K}$  (marked in red and blue respectively). The median values are represented by dashed lines.

a mean value of 1.64 (median is 1.49). The mean value is closer to unity as suggested by the chemical models. Miettinen (2014) reports their HCN/HNC ratio to be in the range 0.15 to 16.6, with a median value of 1.40. These values agree well with our results. The mean value of abundance ratio determined by Zhang et al. (2016) for their sample of high mass stars is seen to be greater than unity (3.91). However, the HCN/HNC abundance ratio is very sensitive to

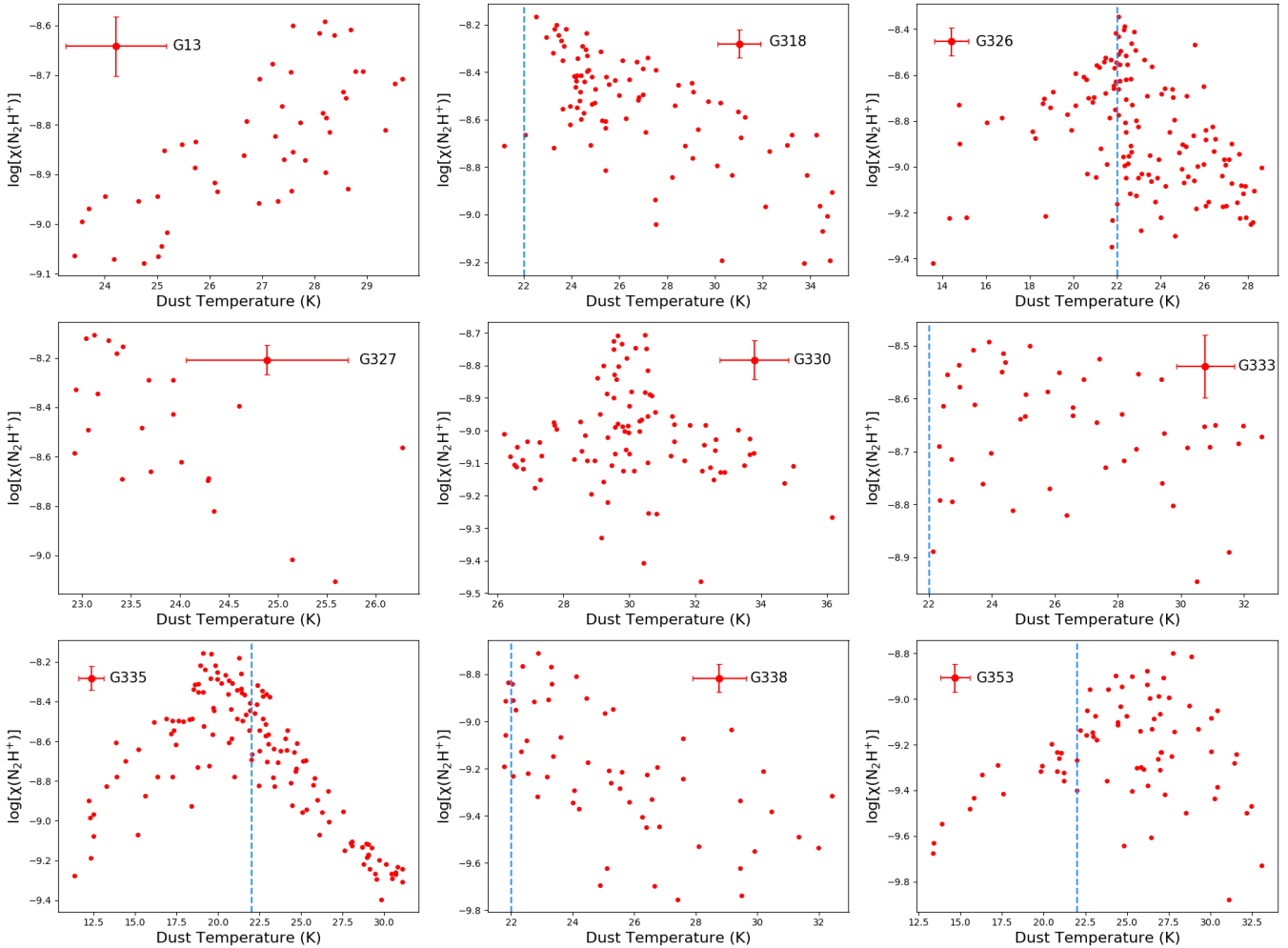


**Figure 9.** The abundance of  $\text{N}_2\text{H}^+$  as a function of dust temperature. The vertical dashed blue line is at  $T_{dust} = 22$  K. Characteristic error bar is shown in the top corner of the plot.

the adopted dust temperatures (Goldsmith et al. 1986; Schilke et al. 1992). While Zhang et al. (2016) have assumed the excitation temperature to be equal to the dust temperature, we find the excitation temperature to be much lower than the dust temperature. The very different abundance ratio of Zhang et al. (2016) may be due to this difference in the value of assumed excitation temperature.

This being said, the HCN/HNC abundance ratio has been shown to vary between regions (Schilke et al. 1992) and this has been attributed to conversion of HNC to HCN at temperatures above  $T \sim 24$  K [see equation (A7)]. The abundance ratio appears to show a variation around 24 K for the pixel-by-pixel case (top panel, Fig. 7). We investigate this further in Fig. 8 which shows the probability distribution functions (PDFs) for the ratios of samples with dust temperatures above and below  $T_{dust} = 24$  K shown in red and blue, respectively. The sample with  $T_{dust} > 24$  K has a higher median ratio, which is in agreement with Schilke et al. (1992) who interpret this increase with source evolution. The lower panel of Fig. 7 shows a decreasing trend with increasing dust temperature, although at  $< 3\sigma$  confidence level based on a Pearson test. We would therefore like to caution against over interpretation of this trend.

We also investigate the variation in  $\text{N}_2\text{H}^+$  abundance with respect to dust temperature, for our sample of MM sources. Fig. 9 shows

the  $\text{N}_2\text{H}^+$  abundance plotted as a function of dust temperature in each pixel of the 9 sources ( $S/N \gtrsim 5$ ). It is seen that for all the sources except G13, the abundances increase till  $T_{dust} \approx 22$  K and then decrease as the temperature increases. The increase in  $\text{N}_2\text{H}^+$  abundances at lower temperatures ( $T < 24$  K) is also observed by Sanhueza et al. (2012), Hoq et al. (2013), Miettinen (2014) and several other studies. This positive correlation is often associated with the enhanced  $\text{N}_2$  evaporation from dust grains, resulting in the formation of more  $\text{N}_2\text{H}^+$  molecules (Chen et al. 2013). As the temperature exceeds 22 K, we see a decline in the abundance of  $\text{N}_2\text{H}^+$ . This is in agreement with the chemical models, which suggest the liberation of CO molecules from the dust grains at  $T_{dust} > 20$  K, causing the depletion of  $\text{N}_2\text{H}^+$  molecules.

#### 4.2 Detection of infall signatures

$\text{HCO}^+$  is one of the suitable candidates for investigating infall motions in both low mass and high mass star forming regions. To distinguish self-absorbed line from other double peaked line profiles, we generally make use of its optically thin isotopologue  $\text{H}^{13}\text{CO}^+$  (Klaassen et al. 2012). Mardones et al. (1997) defined a dimensionless asymmetry parameter  $\delta V$ , to quantify the blue-skewed profiles,

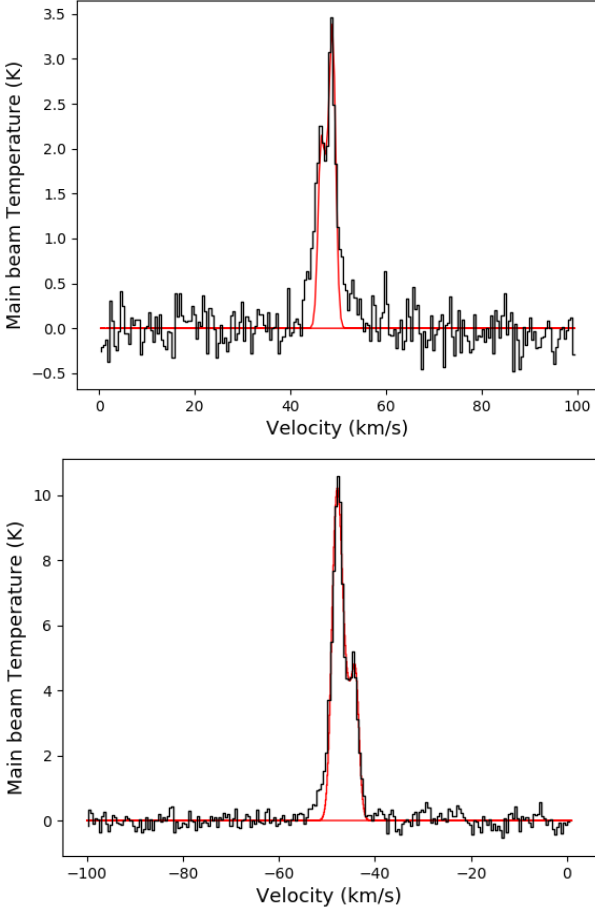


**Figure 10.**  $\text{HCO}^+$  spectrum of a single pixel fitted by "Hill5" model for G13 and G335 (top and bottom panels respectively).

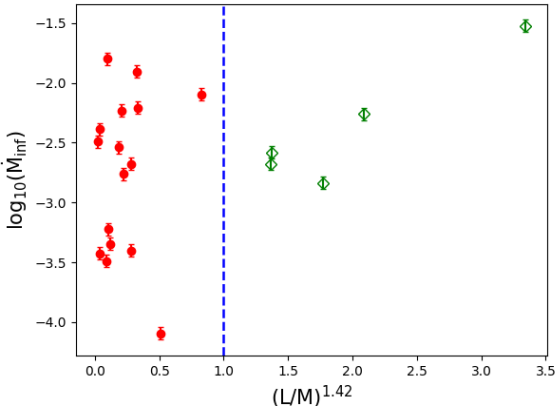


**Figure 11.** Mass infall rates plotted against  $(L/M)^{1.42}$ . The methanol maser hosts that are in accretion phase and clearing phase are shown in red (filled circles) and green (unfilled diamonds) points, respectively. The blue dashed line represents the fit to the 'IR-P' sources in Molinari et al. (2008).

$$\delta V = \frac{V_{thick} - V_{thin}}{\Delta V} \quad (3)$$

Here,  $V_{thick}$  and  $V_{thin}$  represent the LSR velocities of the optically thick and optically thin lines and  $\Delta V$  is the FWHM of the optically thin line. Line profiles with blue asymmetry are characterized by negative values of the asymmetry parameter – i.e.  $\delta V < 0$ . As we do not have any strong ( $> 3\sigma$ )  $\text{H}^{13}\text{CO}^+$  detections, we use optically thin  $\text{N}_2\text{H}^+$  for the calculations. We obtained blue-asymmetries for 21 sources in our sample. In addition, two sources, G13 and G335, displayed a blue asymmetric self-absorbed line profile. The line profiles of these sources were modelled using the radiative transfer model "Hill5" (De Vries & Myers 2005) in order to determine the infall velocity. Fig. 10 illustrates  $\text{HCO}^+$  fitted by "Hill5" model for a single pixel of G13 and G335. For sources that exhibited blue-asymmetry, but not self-absorption, we used  $V_{in} = V_{thin} - V_{thick}$  as an estimate of the infall velocity. The mass infall rate is then computed from the infall velocity as

$$\dot{M}_{inf} = 3 \frac{M_{cl}}{R_{cl}} V_{in} \quad (4)$$

where  $M_{cl}$  and  $R_{cl}$  are the mass and radius of the clumps respectively. These values are taken from Table 3 of Paper I. The mass infall rates calculated, fall in the range  $8.0 \times 10^{-5} \text{ M}_{\odot} \text{ yr}^{-1} - 1.24 \times 10^{-2} \text{ M}_{\odot} \text{ yr}^{-1}$  with median value being  $2.3 \times 10^{-3} \text{ M}_{\odot} \text{ yr}^{-1}$ . The uncertainties in these values are typically less than 15 percent. The calculated infall rates are in good agreement with values that are typically found towards massive star forming regions (Young et al. 1998; Fontani et al. 2002; López-Sepulcre et al. 2010; Saral et al. 2018). Fig. 11 shows  $\dot{M}_{inf}$  as a function of luminosity to mass ( $L/M$ ) ratio. The  $L/M$  ratio serves as a diagnostic tool to infer the evolutionary state of the source. In Fig. 11, the x-axis is  $(L/M)^{1.42}$ , since this represents the fit to the 'IR-P' sources in Molinari et al. (2008) and delineates sources in accretion phase from those in clearing phase (refer Figure 11 of Paper I). The sources belonging to the accretion phase and clearing phase are marked in red and green respectively. Although the mass infall rates appear to show a weak positive correlation with  $L/M$  ratios ( $r = 0.3$ ), this is inconclusive due to  $p\text{-value} > 0.003$ . A larger sample of sources in clearing phase can elucidate the evolutionary effects of infall rates. Wyrowski et al. (2016) report a similar result for their sample of high mass clumps, where 3 of their 8 sources showed higher infall rates towards higher  $L/M$ . He et al. (2016) obtained median mass infall rates of  $(7 - 8) \times 10^{-3} \text{ M}_{\odot} \text{ yr}^{-1}$  for pre-stellar, protostellar and ultra-compact H II regions for their sample of 732 massive clumps and concluded that the infall rates are independent of the evolutionary stage. We also found no significant trends in the mass infall rate when plotted against methanol maser luminosities.

### 4.3 Implications about the evolutionary stage

As indicated earlier in §1, a number of studies (e.g., Ellingsen 2006; Pandian et al. 2010; Billington et al. 2019, and references therein) using continuum emission from radio to infrared wavelengths strongly suggest that 6.7 GHz methanol masers trace an early evolutionary stage of massive star formation, mostly prior to the formation of a H II region. In particular, the mass to luminosity ratio of methanol maser sources are consistent with  $\sim 93\%$  of them being in accretion phase (Paper I). A similar study by Jones et al. (2020) compares the physical properties of clumps associated with maser emission with that of the protostellar sources without maser emission and find the  $L/M$  ratio for maser associated clumps to be slightly higher than that of the latter, suggesting that the maser sources are more evolved.

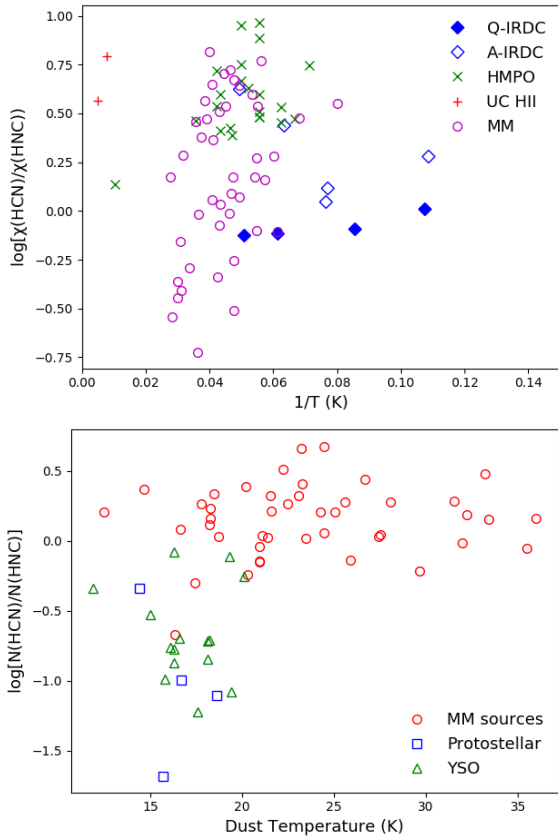


**Figure 12.** MM sources over plotted on results obtained by previous studies. The top panel shows the HCN/HNC ratios derived by [Jin et al. \(2015\)](#) and the bottom panel shows that of [Saral et al. \(2018\)](#).

In this context, it is of interest to see whether the chemical properties of these clumps, examined based on the chemical model, is in agreement with the conclusions derived from their physical properties. Since different molecular species form in specific chemical environments, the ratio of their abundances and intensities can act as a tracer for the evolutionary stage of the high-mass clump. For example, [Rathborne et al. \(2016\)](#) and [Urquhart et al. \(2019\)](#) have observed several line ratios to show systematic trends with source evolution.

We focus on four molecular abundance (intensity) ratios: HCN/HNC, HNC/HCO<sup>+</sup>, N<sub>2</sub>H<sup>+</sup>/HCO<sup>+</sup> and N<sub>2</sub>H<sup>+</sup>/HNC. Here we compare these abundance ratios of our sources with those that are classified to be in different evolutionary stages by earlier studies. We also compare the line intensity ratios of the methanol maser sources with the overall sample of [Rathborne et al. \(2016\)](#) and [Urquhart et al. \(2019\)](#). In this regard, it should be noted that although our data is from the MALT90 survey, our integrated line intensities are in general higher than that of [Rathborne et al. \(2016\)](#). This is primarily due to the differences in spectrum extraction from the data cubes. While we have extracted our spectra from the brightest pixel as discussed in Section 2, [Rathborne et al. \(2016\)](#) use an averaged spectrum, obtained by averaging over 9 pixels around the dust peak. This has the effect of reducing the intensity of the spectrum although the signal to noise ratio can be higher. Our integrated line intensities are also found to be frequently different from those of [Urquhart et al. \(2019\)](#) for the same sources, with the discrepancy most likely arising from differences in the pointing location and velocity resolution ( $\sim 0.9$  km

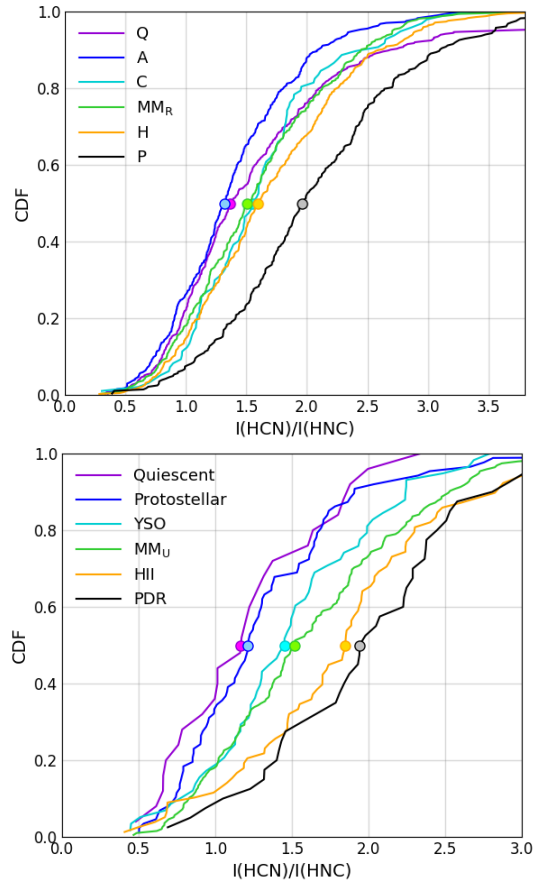


**Figure 13.** MM sources compared with the HCN/HNC integrated intensity ratios of [Rathborne et al. \(2016\)](#) and [Urquhart et al. \(2019\)](#) shown in top and bottom panels respectively. The filled circles on the CDFs represent the median line intensity ratios. Letters ‘Q’, ‘A’, ‘C’, ‘H’ and ‘P’ denotes quiescent, protostellar, compact H II regions, extended H II regions and photo-dissociation regions respectively.

$s^{-1}$ , which is worse than that of MALT90). We hence do not compare the line ratios determined in our work with that of [Rathborne et al. \(2016\)](#) and [Urquhart et al. \(2019\)](#). Rather, we extract the molecular line intensities of methanol maser detections in the MMB from [Rathborne et al. \(2016\)](#) and [Urquhart et al. \(2019\)](#) and compare their ratios with that of sources in other evolutionary states. This is done separately for the sample of [Rathborne et al. \(2016\)](#) and [Urquhart et al. \(2019\)](#). We will refer to the maser sample separated out from [Rathborne et al. \(2016\)](#) and [Urquhart et al. \(2019\)](#) as MM<sub>R</sub> and MM<sub>U</sub> respectively, for the sake of clarity. The minimum, maximum and median values of column density and abundance ratios between different molecules for 68 MM sources are given in Table 5.

We begin by comparing the HCN/HNC abundance ratios with the results of [Jin et al. \(2015\)](#) and [Saral et al. \(2018\)](#). The former estimate the abundance ratio for Infrared dark clouds (IRDCs, quiescent or active, depending on star formation activity), High-mass protostellar objects (HMPOs) and Ultra-compact H II regions (UCHIIs). The latter classify their sources into three evolutionary stages: massive star forming regions (MSF), young stellar objects (YSO) and protostellar. The top panel of Fig. 12 shows that MM sources have similar temperatures as HMPOs but their abundance ratios partially span the IRDC region as well. In contrast, the bottom panel of Fig. 12 shows the abundance ratio to be larger than YSOs and protostellar sources. Fig. 12

**Table 5.** Molecular ratios

Molecular ratios	Min	Max	Median
$N(\text{HCN})/N(\text{HNC})$	0.21	4.76	1.49
$X(\text{HCN})/X(\text{HNC})$	0.21	4.76	1.50
$N(\text{HNC})/N(\text{HCO}^+)$	0.37	7.68	1.17
$X(\text{HNC})/X(\text{HCO}^+)$	0.29	7.68	1.16
$N(\text{N}_2\text{H}^+)/N(\text{HCO}^+)$	0.03	8.71	1.66
$X(\text{N}_2\text{H}^+)/X(\text{HCO}^+)$	0.03	8.71	1.58
$N(\text{N}_2\text{H}^+)/N(\text{HNC})$	0.02	5.73	1.40
$X(\text{N}_2\text{H}^+)/X(\text{HNC})$	0.02	5.73	1.47

Minimum, maximum and median values of different molecular ratios for 68 MM sources. N and X represents column density and abundance respectively.

also shows that the abundance ratio inferred by [Jin et al. \(2015\)](#) differs systematically from that of sources in similar evolutionary stage (e.g. HMPO vs Protostellar or YSO) in [Saral et al. \(2018\)](#). This may be due to the abundance ratio being determined by comparing the column densities of  $\text{H}^{13}\text{CN}$  and  $\text{HN}^{13}\text{C}$  by [Jin et al. \(2015\)](#). Considering that the methodology that we have used in our work is similar to that of [Saral et al. \(2018\)](#), the methanol masers appear to be tracing sources that are more evolved than the protostellar phase. However, due to the small sample size, this result is not statistically significant as inferred by a Kolmogorov-Smirnov (KS) test<sup>6</sup>. In Fig. 13 we compare the cumulative distribution functions (CDFs) of  $\text{HCN}/\text{HNC}$  line intensity ratios of  $\text{MM}_R$  and  $\text{MM}_U$  sources with quiescent, protostellar, H II regions and photo-dominated regions (PDRs) in [Rathborne et al. \(2016\)](#) (top panel) and [Urquhart et al. \(2019\)](#) (bottom panel), respectively. The median value of the ratio for methanol maser sources is seen to be greater than that of protostellar sources, but smaller than that of H II regions/PDRs. Since the  $\text{HCN}/\text{HNC}$  line ratio is seen to increase with source evolution, this suggests that the methanol maser sources are on average more evolved than protostellar sources but less evolved than H II regions/PDRs. The KS test shows the maser sample to be distinct from protostellar sources but not H II regions, showing the former to be a statistically significant result.

[Miettinen \(2014\)](#) compute  $\text{HNC}/\text{HCO}^+$  column density ratios for IR-dark sources and IR-bright sources, whereas [Zhang et al. \(2016\)](#) obtain  $\text{HNC}/\text{HCO}^+$  abundance ratios of prestellar, protostellar and H II/PDR clumps. Both of these studies imply that the  $\text{HNC}/\text{HCO}^+$  ratios decrease as the source evolves. On comparing the values for MM sources with these datasets, we find a higher median column density ratio than IR-dark sources and a lower median abundance ratio than H II/PDR sources. Fig. 14 shows the line intensity ratio of  $\text{HNC}/\text{HCO}^+$  for the classifications of [Rathborne et al. \(2016\)](#) and [Urquhart et al. \(2019\)](#). The line intensity ratio is seen to decline with source evolution, similar to the observation with ratios of column densities. This may be due to enhanced abundance of HNC in colder clumps ([Hoq et al. 2013](#)). Fig. 14 shows that the  $\text{MM}_R$  and  $\text{MM}_U$  sources have a larger median  $I(\text{HNC})/I(\text{HCO}^+)$  than both PDRs and H II regions, and a smaller median ratio than protostellar sources. However, the KS test identifies only methanol maser sources and PDRs to be drawn from separate populations. Hence, we

<sup>6</sup> The null hypothesis considered for KS tests and Student's T tests in this paper is of the two samples being drawn from the same population. We infer two samples to be disparate only if the  $p$ -value  $< 0.003$ , which corresponds to a  $> 3\sigma$  confidence level.

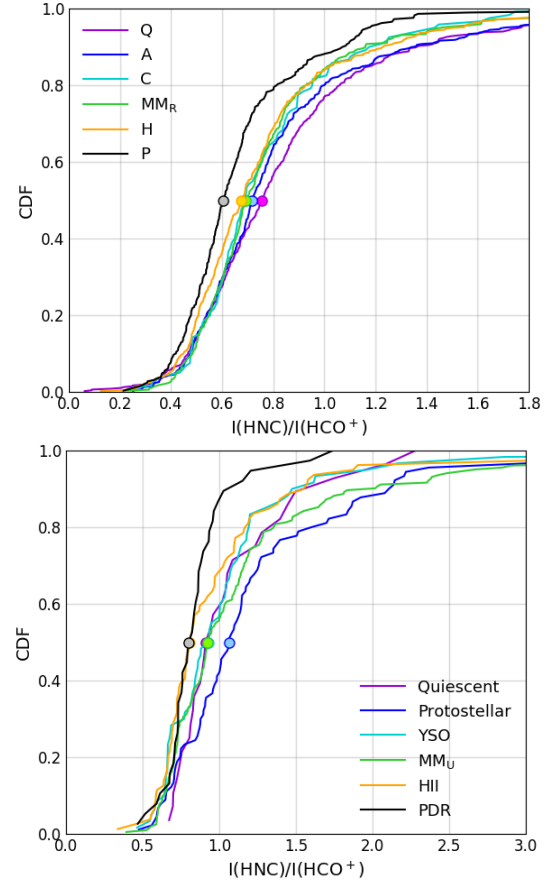


**Figure 14.** Methanol maser sources compared with the  $\text{HNC}/\text{HCO}^+$  integrated intensity ratios of [Rathborne et al. \(2016\)](#) and [Urquhart et al. \(2019\)](#) shown in top and bottom panels respectively. The filled circles on the CDFs represent the median line intensity ratios. Letters ‘Q’, ‘A’, ‘C’, ‘H’ and ‘P’ denotes quiescent, protostellar, compact H II regions, extended H II regions and photo-dissociation regions respectively.

can ascertain that the maser sources are less evolved than PDRs. Comparing with Fig. 13, we can also say that the  $\text{HNC}/\text{HCO}^+$  ratio is not as sensitive as the  $\text{HCN}/\text{HNC}$  ratio in distinguishing between evolutionary states.

It has been reported that  $\text{N}_2\text{H}^+/\text{HCO}^+$  abundance decreases as a high mass clump evolves ([Sanhueza et al. 2012](#); [Lee et al. 2003](#); [Bergin & Tafalla 2007](#)). A comparison with the sources in [Zhang et al. \(2016\)](#) shows that MM sources have a larger median abundance ratio than H II/PDR but lesser than protostellar. We also find that the median abundance ratio of MM sources is higher than that of IR-bright sources in [Miettinen \(2014\)](#). As shown in Fig. 15, we find a higher median ratio for  $\text{MM}_R$  and  $\text{MM}_U$  sources compared to H II regions and PDRs in [Rathborne et al. \(2016\)](#) and [Urquhart et al. \(2019\)](#). Given that the  $\text{N}_2\text{H}^+/\text{HCO}^+$  intensity ratio declines as the source evolves, this is indicative of MM sources being less evolved than H II regions and PDRs. While, a KS test performed on [Urquhart et al. \(2019\)](#) identifies maser sources, protostellar sources and H II regions as distinct samples, the same test performed on [Rathborne et al. \(2016\)](#) identifies maser sources and PDRs as distinct. Hence, [Rathborne et al. \(2016\)](#) suggests maser sources to be less evolved than PDRs and the  $\text{N}_2\text{H}^+/\text{HCO}^+$  line intensity ratios of [Urquhart et al. \(2019\)](#) is consistent with methanol maser sources being at a

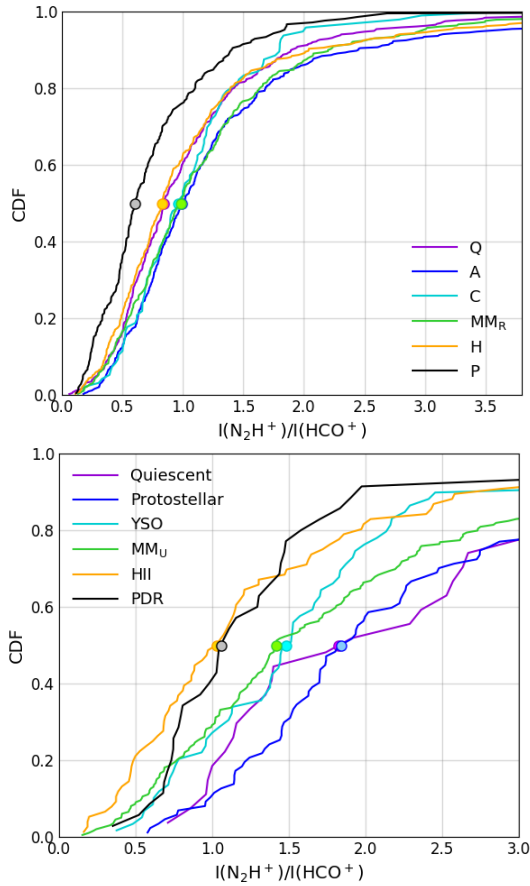


**Figure 15.** MM sources compared with the  $\text{N}_2\text{H}^+/\text{HCO}^+$  integrated intensity ratios of Rathborne et al. (2016) and Urquhart et al. (2019) shown in top and bottom panels respectively. The filled circles on the CDFs represent the median line intensity ratios. Letters ‘Q’, ‘A’, ‘C’, ‘H’ and ‘P’ denotes quiescent, protostellar, compact H II regions, extended H II regions and photo-dissociation regions respectively.

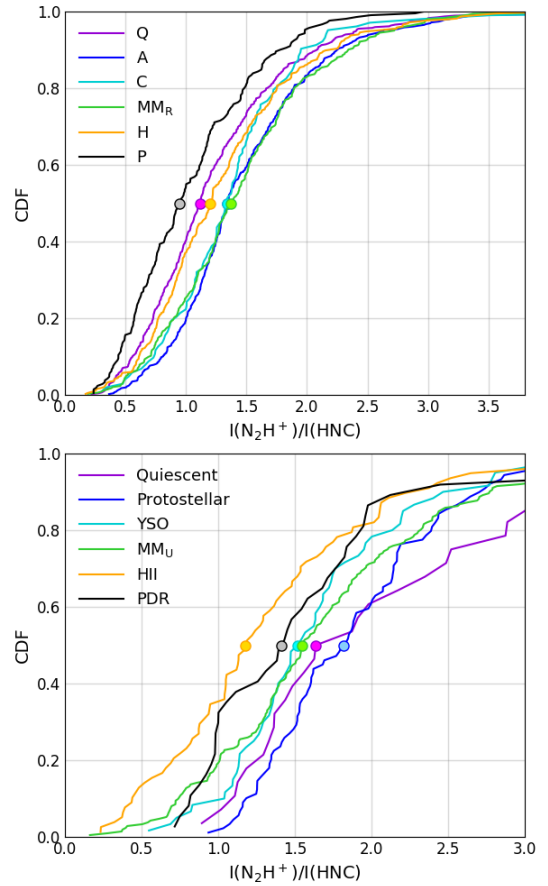


**Figure 16.** MM sources compared with the  $\text{N}_2\text{H}^+/\text{HNC}$  integrated intensity ratios of Rathborne et al. (2016) and Urquhart et al. (2019) shown in top and bottom panels respectively. The filled circles on the CDFs represent the median line intensity ratios. Letters ‘Q’, ‘A’, ‘C’, ‘H’ and ‘P’ denotes quiescent, protostellar, compact H II regions, extended H II regions and photo-dissociation regions respectively.

later evolutionary stage than protostellar phase and less evolved than H II regions.

Finally, we investigate how the  $\text{N}_2\text{H}^+/\text{HNC}$  ratio of MM sources compare with clumps in different evolutionary stages. The median column density and abundance ratios for MM sources are similar to IRDCs in Liu et al. (2013). Fig. 16 shows the  $\text{N}_2\text{H}^+/\text{HNC}$  intensity ratio for sources in different evolutionary stages as per Rathborne et al. (2016) and Urquhart et al. (2019). It can be seen that the  $\text{N}_2\text{H}^+/\text{HNC}$  ratio declines as the source evolves, which is contrary to what was observed by Sanhueza et al. (2012). We also see that the median line ratio of  $\text{MM}_R$  and  $\text{MM}_U$  sources is higher than that of H II regions and PDRs (these are supported by the KS tests), which again is consistent with methanol maser sources tracing an earlier evolutionary stage than H II regions.

In short, the chemical properties are in agreement with the picture of methanol masers tracing an early evolutionary stage prior to the formation of PDRs and possibly H II regions (clearing phase). While the median line ratios of the sources with methanol masers are generally in between that of sources in the protostellar phase and sources identified as H II regions and PDRs, there is considerable overlap in the CDFs. This may be either due to the methanol maser phase overlapping with that of massive young stellar objects and H II regions, or due to chemical properties having lower sensitivity (compared to

continuum studies) with respect to discriminating between different evolutionary phases.

## 5 CONCLUSION

We have investigated the chemical environments of 6.7 GHz methanol maser hosts using  $\text{N}_2\text{H}^+(1-0)$ ,  $\text{HCO}^+(1-0)$ ,  $\text{HCN}(1-0)$  and  $\text{HNC}(1-0)$  molecular lines from the MALT90 survey, where the sources were selected to be representative of the full sample in Paper I. The abundances of these molecular species is in congruence to the typical values observed in massive star forming regions. We do not find any correlation between molecular abundance and dust temperature, which suggest that the molecular abundances do not evolve much during the evolutionary stage traced by methanol masers. The HNC and  $\text{HCO}^+$  integrated intensities, on the other hand, showed a weak positive correlation with source evolution. The  $\text{HCN}/\text{HNC}$ ,  $\text{HNC}/\text{HCO}^+$ ,  $\text{N}_2\text{H}^+/\text{HCO}^+$  and  $\text{N}_2\text{H}^+/\text{HNC}$  ratios are in agreement with the picture of the methanol maser phase occurring prior to the formation of H II regions/PDRs. The analysis of  $\text{HCN}/\text{HNC}$  ratios hint methanol maser sources being more evolved than protostellar sources. These results are consistent with earlier studies including the SED studies of Paper I wherein a majority of the methanol masers

had mass to luminosity ratios suggestive of them being in accretion phase, with the masers turning off in the clearing phase.

## 6 ACKNOWLEDGEMENTS

We thank the anonymous referee whose comments helped in improving the paper. This research has made use of NASA's Astrophysics Data System and VIZIER service operated at CDS, Strasbourg, France. The MATPLOTLIB package (Hunter 2007) for python was used for making plots. We have used the online freemium academic writing environment Overleaf (<https://www.overleaf.com/>) for typesetting this paper.

## 7 DATA AVAILABILITY

The molecular line data can be accessed through the Australia Telescope Online Archive (ATOA) (<http://atoa.atnf.csiro.au/MALT90>). The PACS and SPIRE data is available at the ESA Herschel Science Archive (<http://archives.esac.esa.int/hsa/whsa/>). The ATLASGAL data can be obtained at [https://atlasgal.mpifr-bonn.mpg.de/cgi-bin/ATLASGAL\\_DATASETS.cgi](https://atlasgal.mpifr-bonn.mpg.de/cgi-bin/ATLASGAL_DATASETS.cgi).

## REFERENCES

- Allen T. L., Goddard J. D., Schaefer III H. F., 1980, *The Journal of chemical physics*, 73, 3255
- Bergin E. A., Langer W. D., 1997, *The Astrophysical Journal*, 486, 316
- Bergin E. A., Tafalla M., 2007, *Annu. Rev. Astron. Astrophys.*, 45, 339
- Billington S., et al., 2019, *Monthly Notices of the Royal Astronomical Society*, 490, 2779
- Breen S., Ellingsen S., Contreras Y., Green J., Caswell J., Stevens J., Dawson J., Voronkov M., 2013, *Monthly Notices of the Royal Astronomical Society*, 435, 524
- Caux E., Bottinelli S., Vastel C., Glorian J., 2011, *The Molecular Universe*, 280, 120
- Chen X., Gan C.-G., Ellingsen S. P., He J.-H., Shen Z.-Q., Titmarsh A., 2013, *The Astrophysical Journal Supplement Series*, 206, 22
- De Vries C. H., Myers P. C., 2005, *The Astrophysical Journal*, 620, 800
- Ellingsen S., 2006, *The Astrophysical Journal*, 638, 241
- Fontani F., Cesaroni R., Caselli P., Olmi L., 2002, *Astronomy & Astrophysics*, 389, 603
- Gerner T., Beuther H., Semenov D., Linz H., Vasyunina T., Bühr S., Shirley Y. L., Henning T., 2014, *Astronomy & Astrophysics*, 563, A97
- Giannetti A., et al., 2013, *Astronomy & Astrophysics*, 556, A16
- Goldsmith P., Langer W., Wilson R., 1986, *The Astrophysical Journal*, 303, L11
- Guilloteau S., Baudry A., 1981, *Astronomy and Astrophysics*, 97, 213
- Guzman A. E., Sanhueza P., Contreras Y., Smith H. A., Jackson J. M., Hoq S., Rathborne J. M., 2015, *The Astrophysical Journal*, 815, 130
- He Y.-X., et al., 2016, *Monthly Notices of the Royal Astronomical Society*, 461, 2288
- Hoq S., et al., 2013, *The Astrophysical Journal*, 777, 157
- Hunter J. D., 2007, *Computing in science & engineering*, 9, 90
- Jackson J., et al., 2013, *Publications of the Astronomical Society of Australia*, 30
- Jin M., Lee J.-E., Kim K.-T., 2015, *The Astrophysical Journal Supplement Series*, 219, 2
- Jones B., et al., 2020, *Monthly Notices of the Royal Astronomical Society*, 493, 2015
- Klaassen P., Testi L., Beuther H., 2012, *Astronomy & Astrophysics*, 538, A140
- Ladd N., Purcell C., Wong T., Robertson S., 2005, *Publications of the Astronomical Society of Australia*, 22, 62
- Lee J.-E., Evans II N. J., Shirley Y. L., Tatematsu K., 2003, *The Astrophysical Journal*, 583, 789
- Liu X.-L., Wang J.-J., Xu J.-L., 2013, *Monthly Notices of the Royal Astronomical Society*, 431, 27
- López-Sepulcre A., Cesaroni R., Walmsley C., 2010, *Astronomy & Astrophysics*, 517, A66
- Loughnane R., Redman M., Thompson M., Lo N., O'Dwyer B., Cunningham M., 2012, *Monthly Notices of the Royal Astronomical Society*, 420, 1367
- Mardones D., Myers P., Tafalla M., Wilner D., Bachiller R., Garay G., 1997, *The Astrophysical Journal*, 489, 719
- Mendes M. B., et al., 2012, *The Astrophysical Journal Letters*, 746, L8
- Menten K., Reid M., Pratap P., Moran J., Wilson T., 1992, *The Astrophysical Journal*, 401, L39
- Miettinen O., 2014, *Astronomy & Astrophysics*, 562, A3
- Minier V., Conway J., Booth R., 2001, *Astronomy & Astrophysics*, 369, 278
- Molinari S., Pezzuto S., Cesaroni R., Brand J., Faustini F., Testi L., 2008, *Astronomy & Astrophysics*, 481, 345
- Molinari S., et al., 2010, *Publications of the Astronomical Society of the Pacific*, 122, 314
- Möller T., Endres C., Schilke P., 2017, *Astronomy & Astrophysics*, 598, A7
- Mullins A., Loughnane R., Redman M., Wiles B., Guegan N., Barrett J., Keto E., 2016, *Monthly Notices of the Royal Astronomical Society*, 459, 2882
- Pandian J. D., Momjian E., Xu Y., Menten K., Goldsmith P., 2010, *Astronomy & Astrophysics*, 522, A8
- Paulson S. T., Pandian J. D., 2020, *Monthly Notices of the Royal Astronomical Society*, 492, 1335
- Rathborne J., et al., 2016, *Publications of the Astronomical Society of Australia*, 33
- Sanhueza P., Jackson J. M., Foster J. B., Garay G., Silva A., Finn S. C., 2012, *The Astrophysical Journal*, 756, 60
- Saral G., Audard M., Wang Y., 2018, *Astronomy & Astrophysics*, 620, A158
- Schilke P., Walmsley C. M., Pineau Des Forets G., Roueff E., Flower D. R., Guilloteau S., 1992, *A&A*, 256, 595
- Schlingman W. M., et al., 2011, *The Astrophysical Journal Supplement Series*, 195, 14
- Schuller F., et al., 2009, *Astronomy & Astrophysics*, 504, 415
- Urquhart J., et al., 2019, *Monthly Notices of the Royal Astronomical Society*, 484, 4444
- Wu J., Evans II N. J., 2003, *The Astrophysical Journal Letters*, 592, L79
- Wyrowski F., et al., 2016, *Astronomy & Astrophysics*, 585, A149
- Xu Y., Li J., Hachisuka K., Pandian J., Menten K., Henkel C., 2008, *Astronomy & Astrophysics*, 485, 729
- Young L. M., Keto E., Ho P. T., 1998, *The Astrophysical Journal*, 507, 270
- Zhang Y.-J., et al., 2016, *Astrophysics and Space Science*, 361, 191

## APPENDIX A: CHEMISTRY OF MOLECULES

### A1 HCN,HNC (hydrogen (iso)-cyanide)

HCN and its metastable geometrical isomer HNC are ubiquitous in the dense star forming regions and are considered to be probing high-density gas. They are also good tracers of infall motions in star forming regions (Wu & Evans II 2003). According to gas-phase chemical models, HCN and HNC are primarily produced through the following dissociative recombination reaction of  $\text{HCNH}^+$  (Mendes et al. 2012):



Here both HCN and HNC are formed in equal measures causing HCN/HNC abundance ratio close to unity ( $\approx 0.9$ ). An additional channel where only HNC is produced, is through the dissociative

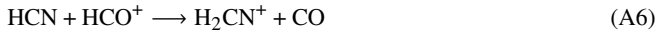
recombination of  $\text{H}_2\text{CN}^+$  and  $\text{H}_2\text{NC}^+$  (Allen et al. 1980):



This results HCN/HNC ratio to slightly rise above unity. These molecules are also formed through other channels say,



These are then followed by rapid isomerisation reactions, once again resulting in near unity HCN/HNC ratio. The destruction of HCN and HNC molecules in dense clouds, primarily happens via the following reaction channels,

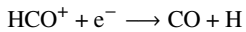


### A2 $\text{HCO}^+$

$\text{HCO}^+$  molecule, regarded as one of the excellent tracers of high-density gas, is mainly formed via the following two channels (Schlingman et al. 2011) :



In the cold dense molecular clouds ( $n > 10^4 \text{ cm}^{-3}$ ,  $T_{kin} < 24 \text{ K}$ ), CO is frozen out on to the dust grains, resulting in the depletion of  $\text{HCO}^+$ . As the temperature increases, CO is liberated from the dust grains, enhancing the production of  $\text{HCO}^+$ . Hence, the column densities and abundances of  $\text{HCO}^+$  molecule is expected to increase as the source evolves. The destruction of  $\text{HCO}^+$  is primarily due to the dissociative recombination reaction:



### A3 $\text{N}_2\text{H}^+$

These molecules are primarily formed through the gas-phase reaction :



and destroyed by the reaction with CO molecules in gas phase producing  $\text{HCO}^+$  Bergin & Langer (1997)



Free electrons can also destroy  $\text{N}_2\text{H}^+$  molecules via the dissociative recombination reaction and it's the primary destruction mechanism when CO is depleted.



## APPENDIX B: COMPARISON OF PROPERTIES OF 68 MM SOURCES WITH THAT OF LARGER MMB SAMPLE

Since the goal of our work is to examine the chemical properties of sources that host 6.7 GHz methanol masers, it is important to ensure that our sample is representative of the Galactic population. To this effect, we have examined the distances, methanol maser luminosities and the FIR luminosity of the host sources of our sample and compared them with that of the full MMB catalogue/sources in Paper I (Fig. B1). While the distribution of distances of our sample is similar to that of the full MMB catalogue and the sample studied in Paper I, there appears to be a slight bias towards larger maser luminosities and FIR luminosities in this study. In order to check for any bias quantitatively, the Student's T-test was performed on the samples. The  $p$ -value obtained was 0.92 for the methanol maser distribution and 0.2 for the FIR luminosity distribution. These are significantly higher than 0.05, which suggests that the differences between the maser populations are not statistically significant.

## APPENDIX C: COMPARISON OF DUST TEMPERATURES OF 68 MM SOURCES WITH THAT OF PREVIOUS WORKS

The left panel of Fig. C1 illustrates the average dust temperature calculated for all the bright pixels ( $S/N \geq 5$ ) of each of the nine source (chosen for pixel-by-pixel study) and average dust temperature calculated for the same sources by (Guzman et al. 2015). Except for two sources, the dust temperature values of the nine sources agree well with what is reported by Guzman et al. (2015). The right panel of Fig. C1 shows the PDFs of dust temperatures of 68 MM sources (taken from Paper I) with that of Guzman et al. (2015). The distributions can be seen comparable with each other.

This paper has been typeset from a  $\text{\TeX}/\text{\LaTeX}$  file prepared by the author.



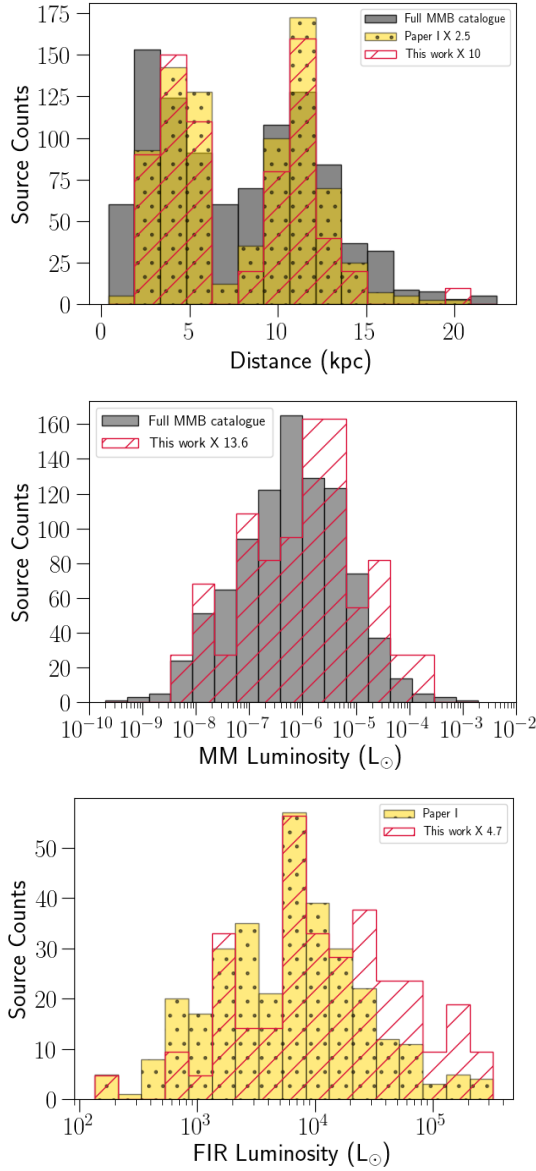


**Figure B1.** The top, middle and bottom panels show the histogram for distances, methanol maser luminosities and FIR luminosities towards the 68 sources of this paper (red with hatches), 321 sources of Paper I (yellow with dots) and the full MMB catalogue (grey). The histograms have been scaled for ease of comparison, with the scale factors being indicated in the legend of each panel.

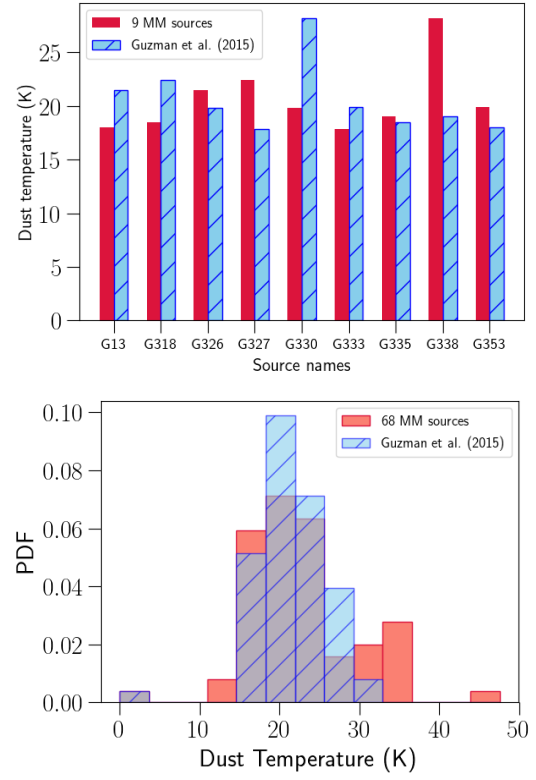


**Figure C1.** Average dust temperatures of sources obtained from pixel-by-pixel fitting of the brightest pixels, compared with the average dust temperatures reported by Guzman et al. (2015), is shown in the left panel. The right panel shows the PDFs of dust temperatures of 68 sources (taken from Paper I) and the average dust temperatures given in Guzman et al. (2015).